Inorganic Chemistry

Article

pubs.acs.org/IC

Microwave-Assisted Synthesis, Microstructure, and Physical Properties of Rare-Earth Chromites

Jesús Prado-Gonjal,[†] Rainer Schmidt,[‡] Juan-José Romero,[§] David Ávila,[†] Ulises Amador,[⊥] and Emilio Morán*[,†]

[†]Departamento Química Inorgánica, Facultad de CC. Químicas, Universidad Complutense de Madrid, 28040 Madrid, Spain

[‡]Departamento Física Aplicada III, Facultad de CC. Físicas, GFMC, Universidad Complutense de Madrid, 28040 Madrid, Spain

[§]Instituto de Cerámica y Vidrio, CSIC, C/Kelsen 5, 28049 Madrid, Spain

[⊥]Departamento Química, Facultad de Farmacia, Universidad San Pablo-CEU, 28668 Boadilla del Monte, Madrid, Spain

Supporting Information

ABSTRACT: The full rare-earth (RE) chromites series (RE)CrO_3 with an orthorhombic distorted (*Pnma*) perovskite structure and the isostructural compound $YCrO_3$ can be synthesized through a simple microwave-assisted technique, yielding high-quality materials. Magnetization measurements evidence that the Néel temperature for antiferromagnetic Cr^{3+}−Cr^{3+} ordering strongly depends on the RE^{3+} ionic radius (IOR), and a rich variety of different magnetic spin interactions exists. Dielectric spectroscopy on sintered pellets indicates electronic inhomogeneity in all samples as manifested by the presence of at least two dielectric relaxation processes associated with grain boundary and grain interior bulk contributions. X-ray diffraction, Raman spectroscopy, and temperature-dependent dielectric permittivity data do not indicate potential noncentrosymmetry in the crystal or concomitant ferroelectricity. Strong correlations between the magnetic and dielectric properties were not encountered, and microwave-synthesized (RE)CrO_3 may not be classified as magnetoelectric or multiferroic materials.

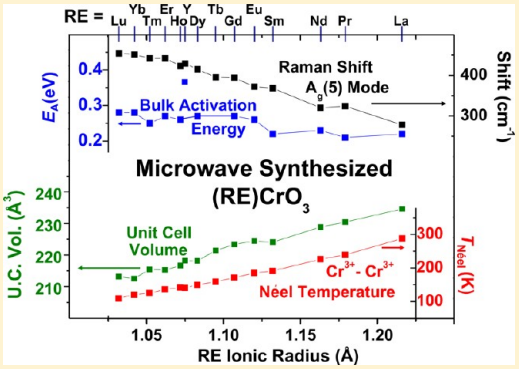

1. INTRODUCTION

Rare-earth (RE) orthochromites (RE)CrO_3 with distorted perovskite structure are currently attracting research interest because of their potential application as multifunctional materials.[1] Chromites in general are under intense investigation nowadays,[2] where the particular interest in the RE species is debited to potential magnetoelectric coupling. Initial studies had claimed that certain rare-earth chromites belong to a new family of ferroelectric and antiferromagnetic multiferroics.[3] Such claims are somewhat surprising though because (RE)-CrO_3 chromites adopt a centrosymmetric orthorhombic structure with space group *Pnma* (No. 62) (frequently given in its nonstandard setting *Pbnm*). Ferroelectricity in centrosymmetric space groups is unusual, and it was attempted recently[4] to explain this by chromium off-centering with a local character and a small value of displacement, leading to weak polarization.[5]

The magnetic properties of the (RE)CrO_3 series contain a rich variety of different magnetic spin interactions, where three different types may occur: (1) Cr^{3+}−Cr^{3+}, (2) Cr^{3+}−$(RE)^{3+}$, and (3) RE^{3+}−RE^{3+}, with isotropic, symmetric, and antisymmetric anisotropic exchange interactions, respectively.[6,7] A weak ferrimagnetic moment in some of the species was claimed to arise from Dzialoshinski−Moriya (D−M) interactions between Cr^{3+} spins.[8,9] The antiferromagnetic Néel temperature T_{N1} for Cr^{3+}−Cr^{3+} ordering increases with the RE cationic radius,[10] which is associated with diminishing lattice distortions and increasing Cr^{3+}−O^{2-}−Cr^{3+} bond angles approaching the ideal 180°.[11]

The charge-transport properties in (RE)CrO_3 materials have been claimed to involve p-type semiconductivity with sensitivity toward humidity, methanol, ethanol, and several gases, which is useful for potential sensor applications.[12,13] Furthermore, $LaCrO_3$ and its doped variants are candidates for application as interconnect materials in solid oxide fuel cells[14,15] and as catalysts for hydrocarbon oxidation.[16]

Usually, rare-earth chromites are synthesized by solid-state reactions where the process involves multiple heating (≥1200 °C) and regrinding steps to help overcome the solid-state diffusion barrier.[17] Other more efficient synthetic methods reported in the literature include self-propagating high-temperature synthesis, metathesis of metal chlorides, decomposition of coprecipitated precursors, a citrate sol−gel route, and hydrothermal synthesis.[18−20] Here in this work we present an alternative route of microwave-assisted synthesis.

In fact, the use of microwaves for the synthesis of solid oxide materials dates back to the late 1980s,[21] although it is only in

Received: September 13, 2012
Published: December 21, 2012

   dx.doi.org/10.1021/ic302000j | *Inorg. Chem.* 2013, 52, 313−320

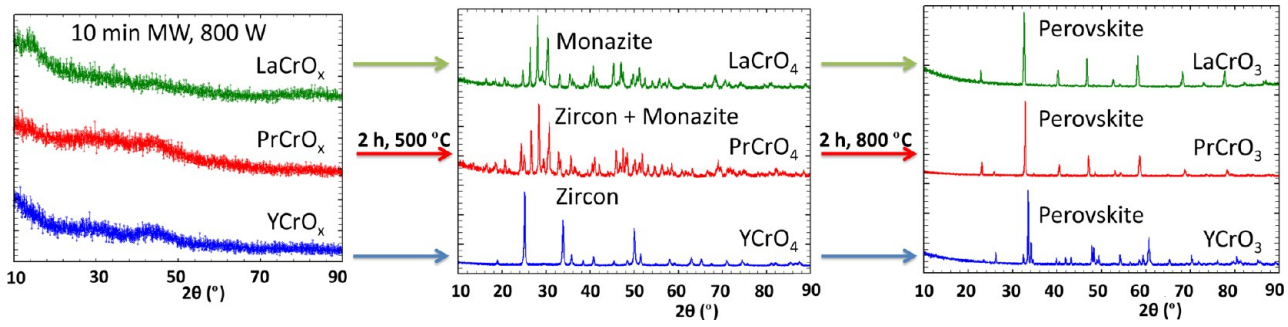

Figure 1. (a) Powder XRD pattern of the MW as-synthesized powders (amorphous), (b) XRD pattern of the 500 °C annealed powders showing monazite ($LaCrO_4$), mixed monazite and zircon ($PrCrO_4$), and a pure zircon ($YCrO_4$) structure, and (c) XRD pattern of the 800 °C annealed powders all showing a pure perovskite phase.

the past decade that this technique has been more widely employed, and plenty of functional materials have recently been synthesized by these means.[22−25] The most commonly applied procedure involves mixing the precursors, pressing them into pellet form, and placing the pellets in a microwave oven in an adequate crucible (usually porcelain, alumina, or SiC). In certain cases of insufficient heating, an additional microwave absorber such as black carbon, graphite, or SiC can be intermixed with the precursor materials to improve coupling between microwaves and material for enhancing microwave energy absorption.[26]

The aim of this work has been to carry out a systematic effort to synthesize the full $(RE)CrO_3$ series including the isostructural compound $YCrO_3$ using microwaves and to perform the structural and microstructural characterization and a detailed investigation of the magnetic and dielectric properties and their correlations with particular focus on possible magnetoelectric or multiferroic behavior.

2. EXPERIMENTAL PROCEDURE

2.1. Synthesis. Appropriate amounts of precursor nitrates [98% $Cr(NO_3)_3{\cdot}9H_2O$ and 99.9% $(RE)(NO_3)_3{\cdot}xH_2O$, Sigma-Aldrich] were weighed and mixed with 5% by weight amorphous carbon acting as a microwave absorber, and the mixture was mechanically homogenized and compacted into pellets of 12 mm diameter.[25] The pellets were placed in a porcelain crucible and irradiated in a domestic microwave oven for 10 min (2.45 GHz and 800 W). Afterwards, the pellets were crushed and the amorphous powder was heated in a conventional furnace in air at 500 °C for 2 h for crystallization to form the precursor $(RE)CrO_4$. Such a precursor was then heated at 800 °C for 2 h to obtain $(RE)CrO_3$. The resulting powders were compacted again into pellets in a 1 ton die press for 5 min, and densification sintering was performed in air at 1300 °C for 15 h.

2.2. Structural and Microstructural Characterization. The phase composition and purity of all precursors and the final products were tested by powder X-ray diffraction (XRD) on a Bruker D8 high-resolution diffractometer using monochromatic Cu $K\alpha_1$ (λ = 1.5406 Å) radiation obtained from a germanium primary monochromator. X-rays were detected with a solid-state rapid LynxEye detector. Structural Rietveld refinements from XRD patterns of all $(RE)CrO_3$ powders were carried out using *FullProf* software.[27]

Field-emission scanning electron microscopy (FE-SEM) of gold-coated powders was carried out using a JEOL 6335F microscope equipped with a detector for energy-dispersive analysis of X-rays (EDAX). Good homogeneity and the expected semiquantitative 1:1 cation compositions of RE/Cr for all powders were confirmed by EDAX. In each sample, analysis was performed on 10 microcrystallites (grains), where the cationic ratios on three different areas of each microcrystallite were measured and the overall average was calculated.

Samples for transmission electron microscopy (TEM) were prepared from powders suspended and ultrasonically dispersed in butanol. One drop of the suspension was placed on a copper grid coated by a holey carbon film. Selected-area electron diffraction and high-resolution TEM (HRTEM) experiments were performed using a JEOL 3000F microscope with a resolution limit of ≈1.1 Å. HRTEM images were recorded with an objective aperture of 70 μm centered on a sample spot within the diffraction pattern area. Fast Fourier transforms (FFTs) of the HRTEM images were carried out to reveal the periodic image contents using the *Digital Micrograph* package.[28] The experimental HRTEM images were also compared to simulated images using *MacTempas* software.[29] Such computations were performed using information from (A) structural parameters obtained from the Rietveld refinement, (B) microscope parameters such as the microscope operating voltage (300 kV) and spherical aberration coefficient (0.6 mm), and (C) specimen parameters such as the zone axis and thickness. The defocus (f) and sample thickness (t) parameters were optimized by assessing the agreement between the model and data, leading to values of f = −33 nm and t = 5 nm.

2.3. Physical Property Measurements. Raman spectroscopy was carried out at room temperature on sintered and polished pellets using a WITec Alpha-300R confocal Raman microscope with a 532 nm laser. A total of 20 measurements were done at different points of each sample to study the possible presence of secondary phases because these could potentially emerge during sintering. Furthermore, investigation of the pellets would allow comparing Raman spectra to dielectric measurements on the search for potential local non-centrosymmetry and ferroelectricity.

Magnetic susceptibility measurements of the synthesized powders were performed in a Quantum Design XL-SQUID magnetometer in the temperature range of 2−300 K at 1 kOe magnetic field. The temperature dependence of the magnetic susceptibility was measured following zero-field-cooled and field-cooled (ZFC−FC) procedures with intermediate demagnetization at room temperature. Ferrimagnetic hysteresis cycles were recorded at 10 K from magnetization versus applied field measurements.

Impedance spectroscopy was carried out on sintered pellets with sputtered gold electrodes between 150 and 550 K using a Novocontrol Alpha-A high-performance frequency analyzer equipped with a liquid-nitrogen-cooled sample chamber. A 100 mV amplitude alternating voltage signal was employed, and the data were recorded between 0.5 Hz and 3 MHz in terms of the real and imaginary parts of the impedance ($Z' - Z''$). The data were converted into the modulus formalism M′−M″ using the standard conversion.[30]

3. RESULTS AND DISCUSSION

3.1. Reaction Pathway. The reaction pathway for $(RE)CrO_3$ formation from nitrate precursors can be described by a three-step process, as indicated by the XRD pattern in Figure 1: (a) formation of an amorphous phase after 10 min of microwave irradiation; (b) formation of polycrystalline (RE)-

dx.doi.org/10.1021/ic302000j | *Inorg. Chem.* 2013, 52, 313−320

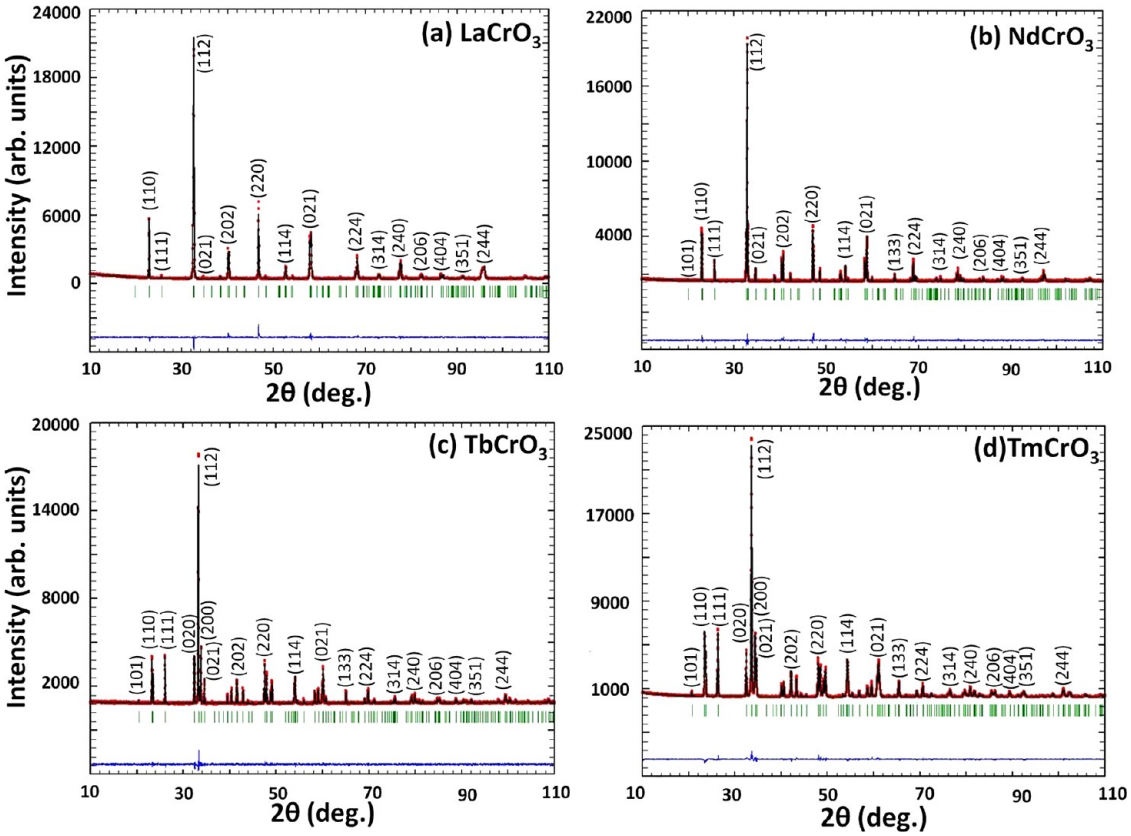

Figure 2. Rietveld refinement of XRD patterns: observed (red dotted lines), refined (black solid lines), and their difference (blue bottom line). Green vertical bars indicate the X-ray reflection positions.

CrO_4 at 500 °C (2 h); (c) formation of (RE)CrO_3 at 800 °C (2 h).

Notably, most of the intermediate (RE)CrO_4 phases show the zircon-type structure with tetragonal symmetry, space group $I4_1/amd$ (No. 141), except in the case of $LaCrO_4$ and $PrCrO_4$. For $LaCrO_4$, the monazite-type structure with monoclinic symmetry, space group $P2_1/n$ (No. 14), is obtained because of the large La^{3+} cationic radius, whereas in $PrCrO_4$, zircon and monazite phases coexist. Another point of interest is the unusual 5+ oxidation state achieved for chromium in this intermediate phase.[31] The (RE)CrO_3 final products adopt a distorted perovskite structure and orthorhombic symmetry, space group *Pnma* (No. 62), upon heating at 800 °C as expected.

3.2. Composition and Crystal Structure. All microwave-synthesized (RE)CrO_3 and $YCrO_3$ powders were single phase, as confirmed by XRD. Figure 2 shows examples of RE chromite XRD patterns and Rietveld refinement fits for RE = La, Nd, Tb, and Tm. The full set of XRD patterns and parameters obtained from the structural refinements are presented in the Supporting Information, Part I, including lattice parameters, atomic positions, bonding angles, and bonding distances.

The distorted perovskite structure with orthorhombic symmetry [space group *Pnma* (No. 62)] was confirmed in all RE chromites, in agreement with previous work.[32,33] The unit cell vectors can be represented by $\sqrt{2}a_p \times 2a_p \times \sqrt{2}a_p$, where a_p refers to the simple cubic perovskite cell. The perovskite tolerance factors for (RE)CrO_3 are t = 0.85−0.93, which is within the reported limits of t = 0.8−1 for perovskite structures of cubic (t = 1) or lower symmetry (t < 1). The cell parameters a, b, and c for the RE family are given in Figure 3 as a function

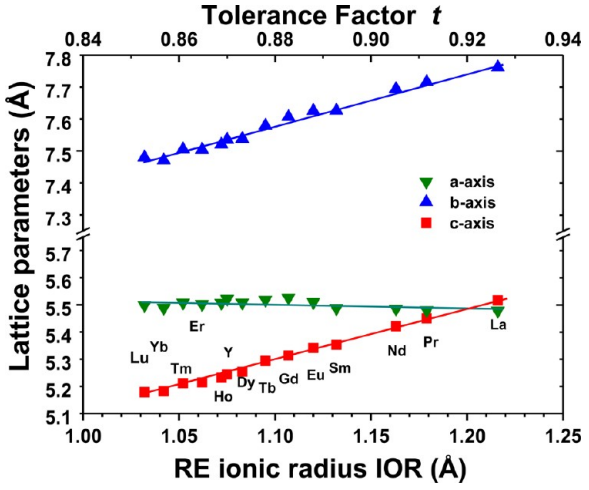

Figure 3. Lattice parameters a, b, and c versus the RE IOR and the perovskite tolerance factor for the (RE)CrO_3 series. An approximately linear increase of b and c with IOR implies an increasing unit cell size.

of the RE ionic radius (IOR) and the tolerance factor t. IOR values were taken from Shannon's tables,[34] where the coordination number 9 was considered for all RE cations consistently. Figure 3 shows an approximately constant cell parameter a, whereas b and c increase with increasing IOR.

It is well-known that XRD is not the optimum technique to deal with structural features related to light atoms such as oxygen; however, some useful structural information was extracted from XRD data, being consistent along the full series (Table 2 in the Supporting Information, Part I). The Cr^{3+}−O^{2-}

dx.doi.org/10.1021/ic302000j | *Inorg. Chem.* 2013, 52, 313−320

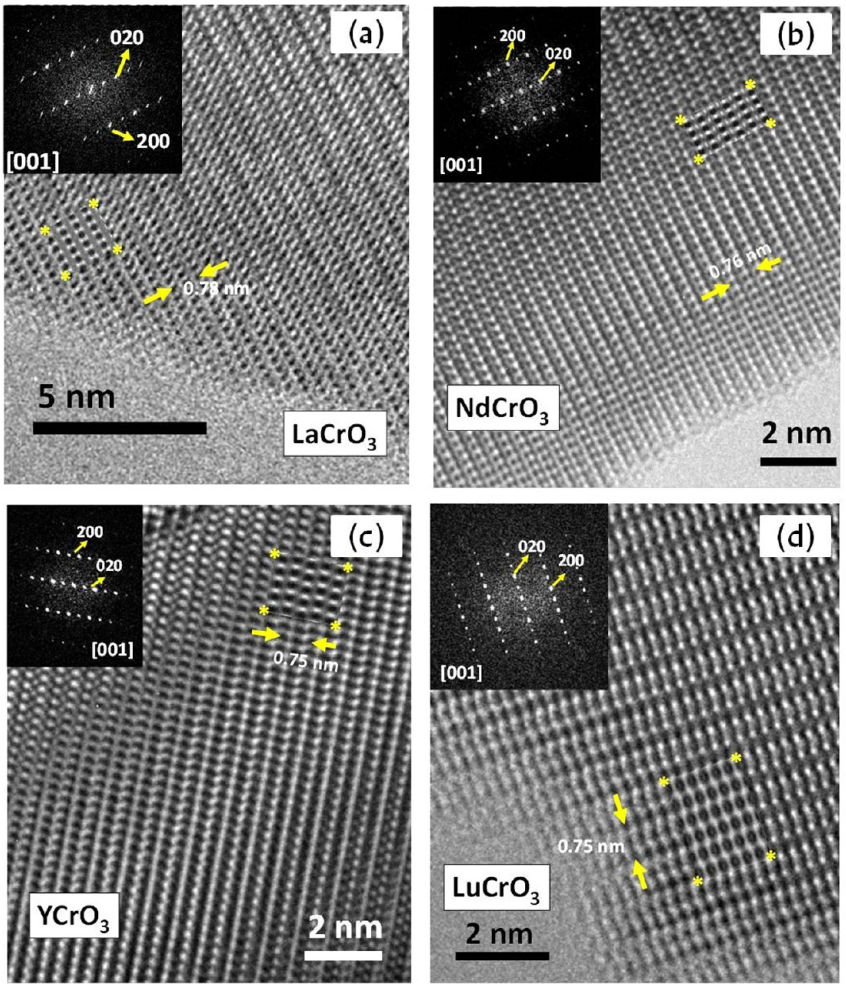

Figure 4. Experimental HRTEM micrographs along the [001] zone axis. No streaking or extra spots are evident (see the FFT images in the figure insets). A good match between experimental and simulated images (rectangles marked by yellow asterisks) is demonstrated.

bonding distances can be determined with relatively low resolution only, but all of these distances appear to be similar (≈1.97 Å) and close to the expected value (1.9805 Å).[35]

The main effect of the RE size is observed in the octahedral tilting of the perovskite cell. θ, φ, and μ represent the tilting angles of the BO_6 octahedra along the three main directions of the ideal ABO_3 cubic perovskite structure, which implies that the larger these angles, the more distorted the structure.[4] All angles decrease quite consistently away from the ideal 180° with decreasing IOR and increasing RE atomic number because the rigid CrO_6 octahedra accommodate A-site RE cations of decreasing size by decreasing the unit cell size and increasing the degree of octahedral tilting.

3.3. Microstructural Characterization. *3.3.1. FE-SEM.* A full set of FE-SEM micrographs for $(RE)CrO_3$ powders is presented in the Supporting Information, Part II, where clear evidence for agglomeration of submicrometer particles is presented.

3.3.2. HRTEM. HRTEM images for $(RE)CrO_3$ (RE = La, Nd, Y, and Lu) are displayed in Figure 4. The experimental images taken along the [001] zone axis show excellent agreement with the simulated images depicted within the rectangles marked with (yellow) asterisks. In all images, the black dots are the projections of the atomic columns from the cationic RE and chromium sublattices, showing a well-ordered crystal without the formation of superstructures or defects such as dislocations and stacking faults. This is evidenced by a regular contrast across the HRTEM images and the absence of extra spots or streaking lines in the FFTs (Figure 4, insets). Enlargements of the HRTEM images with the projected model from each material set on top of the experimental image are displayed in Figure 5 showing good agreement. By careful analysis of the contrast of the images, it can be noticed that the darker dots (RE) and the less darker ones (chromium columns) are oriented in a zigzag fashion along the [010] direction with increasing amplitude in $LaCrO_3$ < $NdCrO_3$ < $YCrO_3$ < $LuCrO_3$. This feature is related to increasing octahedral tilting to accommodate RE cations of decreasing size in the octahedral framework.

3.4. Raman Spectroscopy. Figure 6 shows the Raman spectra of all chromite pellets. No secondary phases could be found on any of the samples, indicating a high degree of material homogeneity. Altogether 24 Raman modes are predicted by group theory for the orthorhombic and centrosymmetric *Pnma* structure with 4 formula units per unit cell.[36] Only 9 of those Raman modes are easily observed in all of the samples (these modes are labeled in Figure 6) because of the measurement range used in this work. Additional symmetrically forbidden Raman modes characteristic of a potential (local) noncentrosymmetry were not encountered, and the observed spectra are in good agreement with a previous study[37] and references therein.

dx.doi.org/10.1021/ic302000j | *Inorg. Chem.* 2013, 52, 313−320

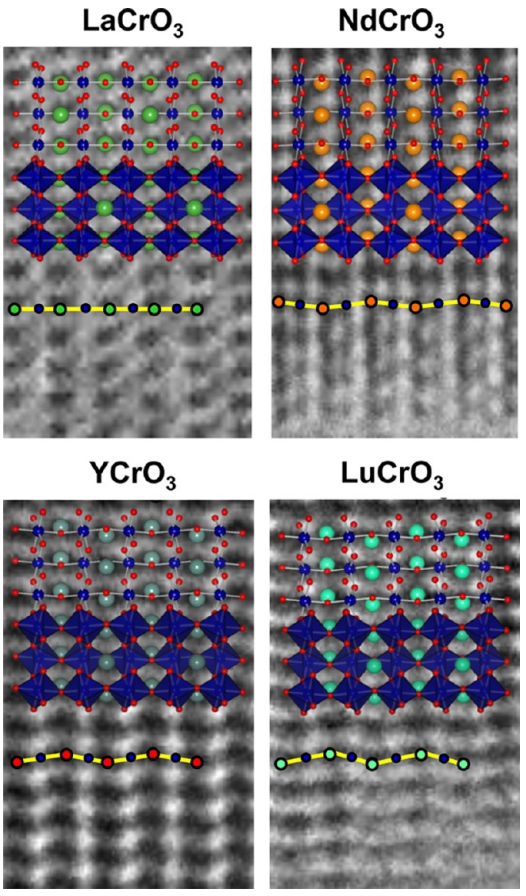

Figure 5. Magnified HRTEM micrographs along the [001] zone axis. The increasing octahedral tilting with decreasing IOR is evidenced by a stronger zigzag orientation of the atoms along the [010] direction.

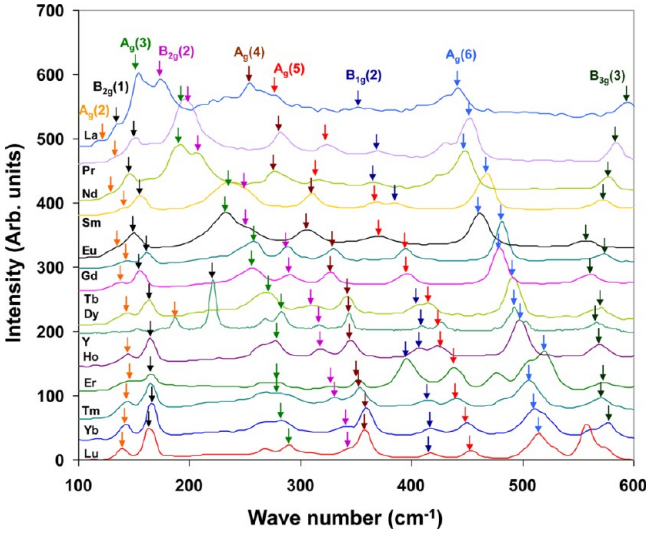

Figure 6. Raman spectra collected at room temperature for the $(RE)CrO_3$ series. Colored arrows indicate different Raman modes and how they develop through the series.

The lower-energy modes (100−200 cm^{-1}) are quite stable across the full series, with the exception of $YCrO_3$. Because these modes are mainly related to the vibrations of the A cations, they are independent of structural changes but highly sensitive to the mass of the cation. Most of the remaining Raman modes show a continuous tendency of decreasing mode position with increasing IOR (see also Supporting Information, Part III), which can be associated with an increase of the unit cell volume. Certain Raman modes display a higher dependence on IOR, for example, the mode $A_g(5)$, which changes from 454 cm^{-1} in $LuCrO_3$ to 278 cm^{-1} in $LaCrO_3$. Furthermore, a mode crossing can be observed between $A_g(5)$ and $B_{1g}(2)$ for samples with IOR between 1.107 Å (Gd) and 1.12 Å (Eu), where both modes are almost indistinguishable. The $A_g(5)$ mode has been previously associated with the [101] rotation of the CrO_6 octahedra and is therefore strongly dependent on the different octahedral tilting angles. A plot of the $A_g(5)$ mode position versus the octahedral tilting angle obtained from Rietveld refinement (θ angle in Tables 2a and 2b of the Supporting Information, Part I) is shown in the Supporting Information, Part III, presenting a linear dependence for all samples (including $YCrO_3$) with a slope of ≈21 cm^{-1}/deg. This value is near to, but slightly smaller than, that previously reported.[37] The $A_g(3)$ Raman mode position also exhibits a linear tendency with the tilting angle with a slope of ≈16 cm^{-1}/deg.

3.5. Magnetic Properties. $(RE)CrO_3$ orthochromites are paramagnetic at room temperature and undergo several magnetic transitions upon cooling. The chromium Cr^{3+}−Cr^{3+} sublattice is first to order at the Néel temperature T_{N1}, which increases monotonically with IOR from 109 K in $LuCrO_3$ to 288 K in $LaCrO_3$, as demonstrated in Figure 7. Upon further

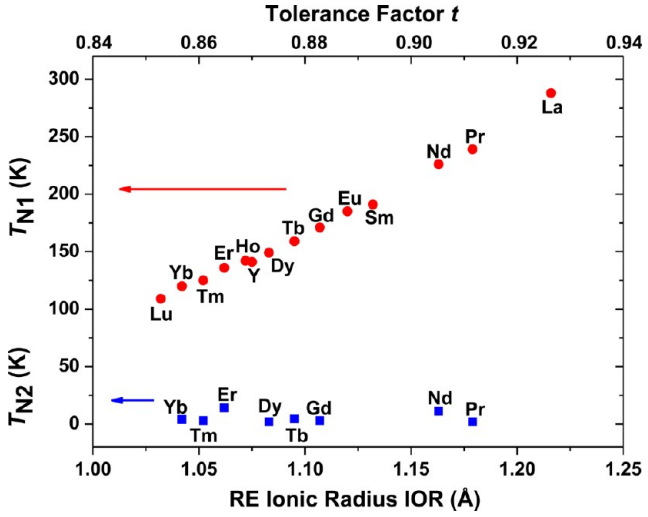

Figure 7. Néel temperature for the Cr^{3+}−Cr^{3+} (T_{N1}) and RE^{3+}−RE^{3+} ordering (T_{N2}) versus the RE IOR and the perovskite tolerance factor. The increasing T_{N1} with IOR reflects increasing tilting angles approaching the ideal 180° Cr^{3+}−O^{2-}−Cr^{3+} angle.

cooling, RE^{3+}−Cr^{3+} interactions appear for certain RE cations, which leads to unusual ZFC−FC magnetic susceptibility (χ) versus temperature (T) characteristics below T_{N1} in the range of ≈50−100 K, as demonstrated in Figure 8. The RE^{3+}−RE^{3+} sublattice orders last at very low temperature (T_{N2}) in the range of ≈2−15 K for certain species, where the variation of T_{N2} does not appear to be correlated with IOR. The χ versus T curves recorded at 1 kOe fall into two different classes according to the magnitude of the magnetic susceptibility χ below T_{N1}. The samples with relatively low χ include RE = Y, La, Nd, Sm, Eu, Tm, Yb, and Lu, whereas χ is higher for RE = Pr, Gd, Tb, Dy, Ho, and Er. Figure 8 shows the temperature dependence of χ for three representative powders each from the low-χ (Figure 8a) and high-χ (Figure 8b) species.

dx.doi.org/10.1021/ic302000j | Inorg. Chem. 2013, 52, 313−320

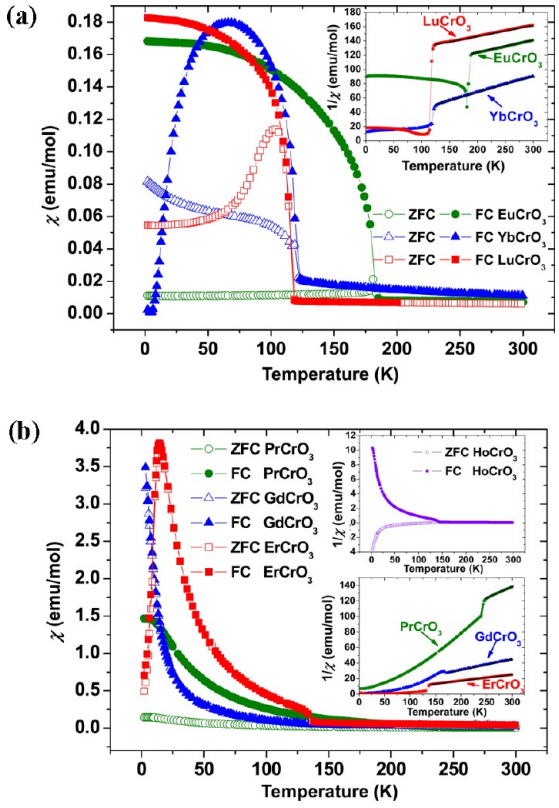

Figure 8. Magnetic susceptibility χ versus temperature T. The data fall into low and high χ regimes. (a) Three representative examples for the low-χ regime. Inset: Inverse magnetic susceptibility $1/\chi$ versus T. Solid lines indicate the Curie–Weiss fits for determining the effective magnetic susceptibility μ_{eff}. (b) Three representative examples for the high-χ regime. Lower inset: Inverse magnetic susceptibility $1/\chi$ versus T. Solid lines indicate the Curie–Weiss fits. Upper inset: $HoCrO_3$ sample exhibiting a peculiar discrepancy between the ZFC and FC curves involving a negative ZFC magnetic susceptibility.

3.5.1. Species with Low Magnetic Susceptibility χ. In Figure 8a, the low-χ representative samples $EuCrO_3$, $YbCrO_3$, and $LuCrO_3$ exhibit a ferrimagnetic moment below T_{N1}, as indicated by clear differences between the ZFC and FC curves. Such a moment is attributed to a small canting angle of the antiferromagnetic Cr^{3+} spins.[38] In the case of $EuCrO_3$ and $LuCrO_3$, the RE magnetic ground state is diamagnetic and, therefore, the low-T magnetic properties are dominated by the Cr^{3+} spin system. The $YCrO_3$, $LaCrO_3$, and $SmCrO_3$ species (data not shown) exhibit features in χ versus T equivalent to $EuCrO_3$, taking into account variation of the Néel temperature T_{N1}, as demonstrated in Figure 7.

The ZFC magnetic susceptibility curve for $YbCrO_3$ exhibits a maximum at 66 K and crosses the ZFC curve at 16 K. This behavior seems unusual because it may suggest that the applied magnetic field during cooling (FC) supports suppression of the low-T magnetism. This finding is in agreement though with previous reports[39] and has been attributed to an antiparallel coupling between the moments of RE = Yb^{3+} and the weak ferrimagnetic component of the Cr^{3+} spins.[40] This behavior could also be involved with a magnetic memory effect. At 4 K, the magnetic susceptibility in FC mode increases modestly, which indicates the onset of antiferromagnetic ordering of Yb^{3+} spins (T_{N2}).

The ZFC–FC curve crossover phenomenon was also observed in $TmCrO_3$ (data not shown), where the FC curve even dropped significantly below zero. Such a negative susceptibility was also encountered in the high-χ species $HoCrO_3$, as discussed below, in that case for the ZFC curve.

3.5.2. Species with High Magnetic Susceptibility χ. The main panel of Figure 8b shows the magnetic properties of $GdCrO_3$, $ErCrO_3$, and $PrCrO_3$ as representative members of the high-χ species. $GdCrO_3$ and $ErCrO_3$ show no significant differences between the ZFC and FC susceptibility curves, and Cr^{3+} ferrimagnetic ordering is not indicated. Contrarily, the $PrCrO_3$ sample does show differences between the ZFC and FC curves appearing below T_{N1} = 239 K, and Cr^{3+} ferrimagnetism is indicated. The RE ordering temperature T_{N2} can be identified by a peaklike structure in the χ versus T curves at $T_{N2} \approx 2$ K.[41] T_{N2} can be identified more clearly in the $ErCrO_3$ sample ($T_{N2} \approx 14$ K), as is the case in $TbCrO_3$ and $DyCrO_3$ (data not shown), whereas the $GdCrO_3$ sample does not reach the T_{N2} peak at low T.

The upper inset in Figure 8b shows the χ versus T curve for $HoCrO_3$, where an unusual negative χ value (diamagnetic-like) is observed at low T in the ZFC curve. Because the negative magnetic susceptibility is unusually high for diamagnetism and seems unphysical, an experimental artifact may seem plausible at first sight. However, this phenomenon can only be observed in the $HoCrO_3$ sample and equivalent reports in the literature have shown precisely the same effect in $HoCrO_3$ only.[42] In ref 42, this extraordinary behavior was interpreted as an interaction between paramagnetic RE^{3+} and canted Cr^{3+} moments, but this argument may be open to debate and, certainly, further work is necessary to clarify this issue, not only in this case but also for the exotic magnetic susceptibility found in $TmCrO_3$ and $YbCrO_3$.

3.5.3. Curie–Weiss Behavior. The lower insets in Figure 8a,b show the temperature dependence of the reciprocal magnetic susceptibility $1/\chi$ for the respective samples. Above T_{N1}, the paramagnetic state follows the Curie–Weiss law: $\chi = C/(T - \Theta)$, where C is the Curie constant related to the effective magnetic moment μ_{eff} and Θ is the Weiss constant. The Curie–Weiss fits are indicated by the solid lines. In the Supporting Information, Part IV, all fitted parameters are summarized and compared to the theoretical values for μ_{eff} from Landolt–Börnstein tables,[43] and generally good agreement is encountered. The Θ values obtained from the fits are all negative, which indicates predominantly antiferromagnetic exchange interactions.

3.5.4. Ferrimagnetic Hysteresis. Figure 9 presents the magnetization versus applied field plots at 10 K for $DyCrO_3$, $HoCrO_3$, and $TmCrO_3$, which all show weak ferrimagnetic hysteresis as a result of Cr^{3+} spin canting. In previous studies, such a weak ferromagnetic moment of the Cr^{3+} spins has been explained with D–M interactions.[8,9]

3.6. Dielectric Properties. Impedance spectroscopy data for the $(RE)CrO_3$ series were collected from sintered pellets. Selected impedance spectra are shown in Figure 10 in terms of the complex impedance plane plot of $-Z''$ versus Z'. The spectra for the Ho-, Gd-, Pr-, and Y-containing samples are normalized and shifted up the Z'' y axes by increasing amounts for demonstration purposes. For the different compositions, two or three semicircles are displayed in $-Z''$ versus Z', which is consistent with two or three conventional dielectric relaxation processes in series.[32,44] Not all semicircles are fully developed, and considerable overlap occurs, which is highlighted in the spectrum for $TmCrO_3$ by the dotted semicircles. All semicircles in Figure 10 are slightly suppressed in a way such that the

dx.doi.org/10.1021/ic302000j | Inorg. Chem. 2013, 52, 313–320

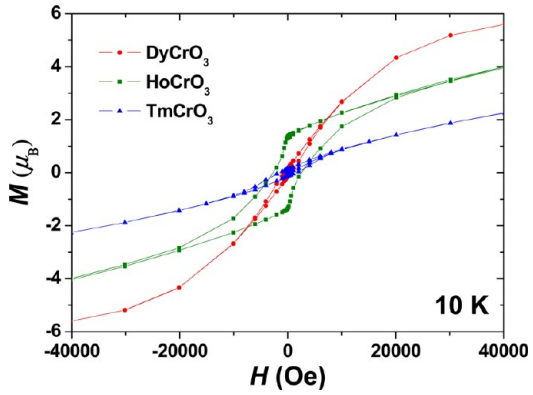

Figure 9. Magnetization versus applied magnetic field H curves at 10 K for three representative species from the (RE)CrO_3 series.

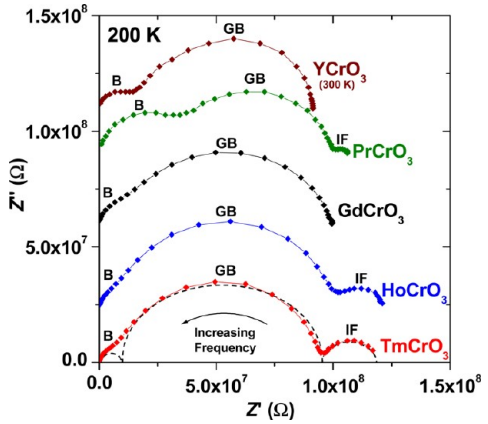

Figure 10. Plots of the imaginary versus real part of the impedance ($-Z''$ vs Z') at 200 K for five representative examples from the (RE)CrO_3 series. $YCrO_3$ data are shown for 300 K. The Ho-, Gd-, Pr-, and Y-containing samples were shifted up the y axis for demonstration purposes. The overlapping of several semicircles is highlighted by the dotted lines in the $TmCrO_3$ spectrum, where each semicircle can be associated with a Bulk (B), grain boundary (GB) or interface (IF) effect.

semicircle center seems to be slightly suppressed below the Z' x axis. This indicates a certain degree of nonideality of the relaxation process, which can be associated with a broadening of the distribution of dielectric relaxation times τ.[30,45]

The two semicircles at high and intermediate frequencies are associated with intrinsic bulk (B) and extrinsic grain boundary (GB) relaxation processes, respectively. In the case of the Tm-, Ho-, and Pr-containing samples, a third semicircle at low frequency is associated with an electrode−sample interface (IF) effect, which also occurs in the, Nd-, Sm-, Dy-, Er-,[25] Yb-, and Lu-containing species.

To extract the resistivity ρ and relative dielectric permittivity ε values for the B and GB relaxations from impedance spectroscopy data for each (RE)CrO_3 sample, equivalent circuit fitting[25] was attempted but did not succeed for all samples. Therefore, ρ and ε values for B and GB contributions were extracted from the respective impedance spectra by a manual procedure to be identical for all samples to render the extracted parameters comparable to each other. Such a procedure is described in detail in the Supporting Information, Part V.

3.6.1. Temperature Trends of Dielectric Parameters. The B and GB resistivity values ρ_1 and ρ_2 are plotted on Arrhenius axes, showing good linearity for all (RE)CrO_3 samples (see the Supporting Information, Part V). From the slopes of such graphs, the B and GB activation energies E_A can be determined and are plotted versus IOR in Figure 11 (upper curves).

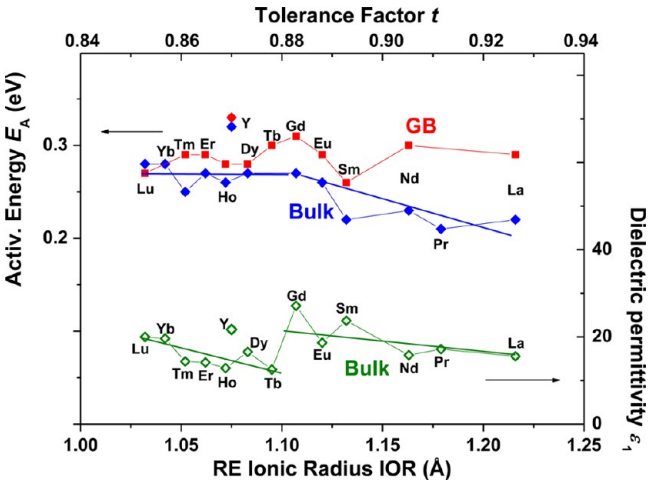

Figure 11. B and GB charge-transport activation energies E_A and bulk dielectric permittivity ε_1 plotted versus IOR and the perovskite tolerance factor.

Although the absolute ρ_1 and ρ_2 values at 200 K and other example temperatures do not show any clear trends with IOR (see the Supporting Information, Part V), the E_A values are quite consistent. Especially, the intrinsic bulk E_A trend seems to show a slight decrease with increasing IOR above the Gd sample, whereas for lower IOR, the bulk E_A trend appears approximately constant. A similar trend is observed in the intrinsic permittivity ε_1 versus IOR (lower curve in Figure 11), where again the trend seems to change near the Gd sample. The $YCrO_3$ sample, on the other hand, falls out of all of the ρ and ε trends presented in Figure 11, which is consistent with the trends in the effective magnetization μ_{eff}. Equivalent to the argument mentioned above, the RE electron configuration seems to play a major role here in determining the electronic charge-transfer rate (resistivity) and the electron cloud polarizability (permittivity) in (RE)CrO_3 chromites.

Most importantly, the permittivity ε_1 values are all relatively low and the electron cloud polarizability may well be the only contribution to the overall measurable polarizability in the (RE)CrO_3 series. Furthermore, the ε_1 values determined did not show any clear temperature dependence (see the Supporting Information, Part V). Therefore, a contribution from an ionic displacement to the overall polarizability, typical for ferroelectricity, is unlikely, and previous reports on ferroelectricity in these materials cannot be confirmed. The absence of ferroelectricity may be consistent though with the centrosymmetric space group used for Rietveld refinements of XRD patterns and the Raman spectra presented here. None of the trends of the magnetic parameters (T_{N1}, T_{N2}, and μ_{eff}) versus IOR are correlated with any of the trends of the dielectric parameters (E_A and ε_1) versus IOR, and obvious magnetoelectric coupling effects are not indicated.

4. CONCLUSIONS

The perovskite (RE)CrO_3 series was synthesized by microwave-assisted methods. A comprehensive characterization in terms of the structural and physical properties was performed. The b and c unit cell parameters showed a consistent increase

dx.doi.org/10.1021/ic302000j | Inorg. Chem. 2013, 52, 313−320

with increasing IOR of the RE cation. The concomitant increase in the octahedral tilting angle approaching 180° resulted in a consistent increase of the $Cr^{3+}-Cr^{3+}$ antiferromagnetic ordering temperature T_{N1}. The magnetic susceptibility χ versus temperature characteristics revealed a rich variety of different spin interactions. The intrinsic bulk charge-transport activation energy and bulk dielectric permittivity in sintered ceramics showed a change in the trend with IOR near the Gd-containing sample. No clear correlations of the magnetic and dielectric properties were found, and major magnetoelectric coupling effects could not be detected. No indications for a noncentrosymmetric space group and associated ferroelectricity were detected from XRD pattern, Raman spectroscopy, and temperature-dependent dielectric permittivity data. Microwave-synthesized $(RE)CrO_3$ chromites may therefore not be classified as magnetoelectric or multiferroic materials.

■ ASSOCIATED CONTENT

Supporting Information

XRD pattern and Rietveld refinement parameters, SEM image, Raman and dielectric spectroscopy, and magnetic structure. This material is available free of charge via the Internet at http://pubs.acs.org.

■ AUTHOR INFORMATION

Corresponding Author

*E-mail: emoran@quim.ucm.es.

Notes

The authors declare no competing financial interest.

■ ACKNOWLEDGMENTS

J.P.-G. acknowledges financial help from the Community of Madrid (Materyener S2009/PPQ-1626) and a Ph.D. scholarship from the Universidad Complutense de Madrid. R.S. acknowledges the Ministerio de Ciencia e Innovación (MICINN) for granting a Ramon y Cajal Fellowship. Furthermore, this work was supported by the MICINN through Grants MAT 2007-31034 and MAT 2010-19837-CO6-01 and -03 . The authors express their gratitude to Dr. Emma McCabe for a critical reading of the manuscript and to Prof. Jacobo Santamaria and Prof. Carlos León for allowing use and assistance with the IS facilities.

■ REFERENCES

(1) Sardar, K.; Lees, M. R.; Kashtiban, R. J.; Sloan, J.; Walton, R. I. *Chem. Mater.* **2011**, *23*, 48.
(2) Belik, A. A.; Matsushita, Y.; Tanaka, M.; Takayama-Muromachi, E. *Chem. Mater.* **2012**, *24*, 2197.
(3) Sahu, J. R.; Serrao, C. R.; Ray, N.; Waghmare, U. V.; Rao, C. N. R. *J. Mater. Chem.* **2007**, *17*, 42.
(4) Mitchell, R. H. *Perovskites modern and ancient*; Almaz Press Inc.: Thunder Bay, Ontario, Canada, 2002; p 20.
(5) Ramesha, K.; Llobet, A.; Proffen, Th.; Serrao, C. R.; Rao, C. N. R. *J. Phys.: Condens. Matter* **2007**, *19*, 102202.
(6) Su, Y.; Zhang, J.; Feng, Z.; Li, L.; Li, B.; Zhou, Y.; Chen, Z.; Cao, S. *J. Appl. Phys.* **2010**, *108*, 013905.
(7) Cooke, A. H.; Martin, D. M.; Wells, M. R. *J. Phys. C: Solid State Phys.* **1974**, *7*, 3133.
(8) Dzialoshinski, I. *J. Phys. Chem. Solids* **1958**, *4*, 241.
(9) Moriya, T. *Phys. Rev.* **1960**, *120*, 91.
(10) Shamir, N.; Shaked, H.; Shtrikman, S. *Phys. Rev. B* **1981**, *24*, 6642.
(11) Jaiswal, A.; Das, R.; Vivekanand, K.; Maity, T.; Abraham, M.; Adyanthaya, S.; Poddar, P. *J. Appl. Phys.* **2010**, *107*, 013912.
(12) Russo, N.; Mescia, D.; Fino, D.; Saracco, G.; Specchia, V. *Ind. Eng. Chem. Res.* **2007**, *46*, 4226.
(13) Tsushima, K.; Aoyagi, K.; Sugano, S. *J. Appl. Phys.* **1970**, *41*, 1238.
(14) Fergus, J. W. *Solid State Ionics* **2004**, *171*, 1.
(15) Prado-Gonjal, J.; Arévalo-López, Á. M.; Morán, E. *Mater. Res. Bull.* **2011**, *46*, 222.
(16) Beckers, J.; Rothenberg, G. *Chem. Phys. Chem.* **2005**, *6*, 223.
(17) Satoh, H.; Koseki, S.-i.; Takari, M.; Chung, W. Y.; Kamegashira, N. *J. Alloys Compd.* **1997**, *259*, 176.
(18) Kuznetsov, M. V.; Parkin, I. P. *Polyhedron* **1998**, *17*, 4443.
(19) Parkin, I. P.; Komarov, A. V. *Polyhedron* **1996**, *15*, 3117.
(20) Rivas-Vázquez, L. P.; Rendón-Angeles, J. C.; Rodríguez-Galicia, J. L.; Gutiérrez-Chavarria, C. A.; Zhu, K. J.; Yanagisawa, K. *J. Eur. Ceram. Soc.* **2006**, *26*, 81.
(21) Baghurst, D. R.; Mingos, D. M. P. *J. Chem. Soc., Chem. Commun.* **1988**, 829.
(22) Parada, C.; Morán, E. *Chem. Mater.* **2006**, *18*, 2719.
(23) Prado-Gonjal, J.; Schmidt, R.; Ávila, D.; Amador, U.; Morán, E. *J. Eur. Ceram. Soc.* **2012**, *32*, 611.
(24) Gómez, I.; Hernández, M.; Aguilar, J.; Hinojosa, M. *Ceram. Int.* **2004**, *30*, 893.
(25) Aguilar-Garib, J.; Garcia, F.; Valdez, Z. *J. Ceram. Soc. Jpn.* **2009**, *117*, 801.
(26) Mingos, D. M. P.; Baghurst, D. R. *Chem. Soc. Rev.* **1991**, *20*, 1.
(27) Rodríguez-Carvajal, J. *Physica B* **1993**, *192*, 55 (http://www.ill.eu/sites/fullprof/).
(28) *Digital Micrograph*, 1.71.38; Gatan, Inc.: Pleasanton, CA, 2010.
(29) Kilaas, R. *MacTempas Software*, version 2.3.7; Total Resolution Inc.: Berkeley, CA, 1988.
(30) Barsukov, E. J.; Macdonald, R. *Impedance Spectroscopy: Theory, Experiment and Applications*; John Wiley & Sons Inc.: Hoboken, NJ, 2005.
(31) Jiménez, E.; Torralvo, M. J.; Isasi, J.; Sáez-Puche, R. *Chem. Educ.* **2003**, *8*, 1.
(32) Geller, S. *Acta Crystallogr.* **1957**, *10*, 243.
(33) Subba Rao, G. V.; Wanklyn, B. M.; Rao, C. N. R. *J. Phys. Chem. Solids* **1971**, *32*, 345.
(34) Shannon, R. D. *Acta Crystallogr.* **1976**, *A32*, 751.
(35) García-Lastra, J. M.; Barriuso, M. T.; Aramburu, J. A.; Moreno, M. *Phys. Rev. B* **2008**, *78*, 085117.
(36) Iliev, M. N.; Abrashev, M. V.; Lee, H. G.; Popov, V. N.; Sun, Y. Y.; Thomsen, C.; Meng, R. L.; Chu, C. W. *Phys. Rev. B* **1998**, *57*, 2872.
(37) Weber, M. C.; Kreisel, J.; Thomas, P. A.; Newton, M.; Sardar, K.; Walton, R. I. *Phys. Rev. B* **2012**, *85*, 054303.
(38) Widatallah, H. M.; Al-Harthi, S. H.; Johnson, C.; Klencsar, Z.; Gismelseed, A. M.; Moore, E. A.; Al-Rawas, A. D.; Wynter, C. I.; Brown, D. E. *J. Phys. D: Appl. Phys.* **2011**, *44*, 265403.
(39) Su, Y.; Zhang, J.; Feng, Z.; Li, L.; Li, B.; Zhou, Y.; Chen, Z.; Cao, S. *J. Appl. Phys.* **2010**, *108*, 013905.
(40) Kojima, N.; Tsushima, K.; Kurita, S.; Tsujikawa, I. *J. Phys. Soc. Jpn.* **1980**, *49*, 1456.
(41) Laar, B. V.; Elemans, B. A. A. *J. Phys. (Paris)* **1971**, *32*, 301.
(42) Su, Y. L.; Zhang, J. C.; Li, L.; Feng, Z. J.; Li, B. Z.; Zhou, Y.; Cao, S. X. *Ferroelectrics* **2011**, *410*, 102.
(43) Goodenough, J. B.; Longo, J. M. In *Landolt–Börnstein New Series III*; Hellwege, K.-H., Hellwege, A. M., Eds.; Springer: Berlin, 1970; Vol. *4*, Part a, p 228.
(44) Irvine, J. T. S.; Sinclair, D. C.; West, A. R. *Adv. Mater.* **1990**, *2*, 132.
(45) Schmidt, R.; Eerenstein, W.; Winiecki, T.; Morrison, F. D.; Midgley, P. A. *Phys. Rev. B* **2007**, *75*, 245111.